Technical Report no. 1088 (ISSN 1135-9420): Direct numerical simulation of sediment transport in a horizontal channel

M. Uhlmann

Unidad de Modelización de Procesos
CIEMAT
Avenida Complutense 22, 28040 Madrid (Spain)
markus.uhlmann@ciemat.es

August 9, 2006

Abstract. We numerically simulate turbulent flow in a horizontal plane channel over a bed of mobile particles. All scales of fluid motion are resolved without modeling and the phase interface is accurately represented. Our results indicate a possible scenario for the onset of erosion through collective motion induced by buffer-layer streaks.

Contents

1 Introduction

The motion of rigid particles suspended in horizontal boundary-layer-type flow is a feature which is encountered in a wide range of applications of technological and environmental interest. Examples include pneumatic conveying and bedload transport in rivers. In the latter case, inhomogeneous particle transport leads to a modification of the shape of the bed, and an accurate prediction of the erosion process is often desirable for engineering purposes. The basic question in this context concerns the critical conditions for the onset of erosion, most commonly described in terms of the Shields diagram (a fit of experimental data represented in terms of the non-dimensional shear stress vs. the normalized particle diameter). However, up to this date the detailed mechanisms giving rise to the particular shape of the critical curve have not been satisfactorily explained.

In the present study we approach this problem by generating flow data with the aid of direct numerical simulations (DNS). This technique enables us to analyze any quantity of interest with great spatial and temporal precision, albeit at a large computational cost and for somehow idealized situations. DNS can generally be regarded as a complement to laboratory experiments.

First, let us mention a selection of relevant experimental work. Kaftori, Hetsroni and Banerjee have studied the motion of particles in a horizontal turbulent boundary layer [2, 3]. In these experiments, particles were nearly buoyant, and their interaction with the coherent structures of the near-wall region was documented in detail. By analysis of high-speed video images, Niño and Garcia [4] have identified the upward motion downstream of strong inclined shear layers as the dominant mechanism which lifts heavy particles away from the wall in turbulent open channel flow. Niño, Lopez and Garcia [5] present parametrical data for the onset of erosion. Their results will be used below for the purpose of quantitative comparison. Kiger and Pan [6] found evidence for a correlation between the existence of hairpin vortex packets and vertical motion of heavy particles.

Reliable numerical studies of particulate flow have only recently come into reach of available supercomputing capabilities. DNS of turbulent flow of roughness elements has been performed e.g. by Leonardi *et al.* [7]. Zeng, Balachandar and Fischer have studied the forces acting upon a sphere which translates parallel to a wall in a quiescent fluid [8]. Patankar *et al.* have studied the lift-off of a single circular disc in horizontal (laminar) Poiseuille flow [9]. In a companion paper, Choi and Joseph have simulated the fludization of 300 closely packed circular discs in the same configuration [10]. They found that—for sufficiently high values of the driving pressure gradient—the bed of particles is "inflated" in an early stage (meaning that fluid enters the bed) which in turn causes dislocation of individual particles in the top row, finally leading to full resuspension of particles. It should be noted that the particles were located on a smooth wall. Furthermore, it is not clear whether their conclusions extend to the three-dimensional case. Finally, it should be kept in mind that the flow was laminar, which means that there are potentially less mechanisms available for the lift-off of particles.

Pan and Banerjee [11] were probably the first to conduct DNS of turbulent plane channel flow with suspended particles. In their case the orientation of the mean flow direction was horizontal. However, they mainly considered fixed particles and the spatial resolution of each sphere was rather coarse. The particles in their study were nearly neutrally buoyant, and, therefore, the mechanism for re-suspension was not considered.

To our knowledge, the re-suspension of heavy spherical particles in horizontal turbulent channel flow has not previously been studied using the DNS approach. In the following we will first outline our numerical method. In § 3.1-3.2 we will present the results of preliminary computations of a single fixed sphere in laminar plane channel flow and of turbulent flow over a smooth wall in a half-channel configuration. In § 3.3 we turn to the problem of turbulent flow over a double layer of spherical roughness elements, before discussing the numerical experiments of the erosion of particles in § 3.4. A discussion of our results can be found in § 4.

2 Numerical method

The numerical method which we will use for the direct simulation of sediment transport has been proposed in [12]. For clarity we will first present the general idea in the framework of a single-step time discretization. The final algorithm as implemented in the code SUSPENSE (Suspended Particle Evolution by Navier-Stokes Equations) will be given in equation (6) below. For this purpose, let us write the momentum equation in the following form

$$\frac{\mathbf{u}^{n+1} - \mathbf{u}^n}{\Delta t} = \mathbf{rhs}^{n+1/2} + \mathbf{f}^{n+1/2}\,, \tag{1}$$

where $\mathbf{rhs}^{n+1/2}$ regroups all usual forces (convective, pressure-related, viscous) and $\mathbf{f}^{n+1/2}$ is the fluid-solid coupling term, both evaluated at some intermediate time level. Since the work of [13] it is common to express the additional force by simply rewriting the above equation as

$$\mathbf{f}^{n+1/2} = \frac{\mathbf{u}^{(d)} - \mathbf{u}^n}{\Delta t} - \mathbf{rhs}^{n+1/2} \tag{2}$$

where $\mathbf{u}^{(d)}$ is the desired velocity at any point where forcing is to be applied (i.e. at a point inside a solid body). Formula (2) is characteristic for direct forcing methods. Problems arise from the fact that in general the solid-fluid interface does not coincide with the Eulerian grid lines, meaning that interpolation needs to be performed in order to obtain an adequate representation of the interface. In [12] the definition of the force term was instead formulated at Lagrangian positions attached to the surface of the particles, viz.

$$\mathbf{F}^{n+1/2} = \frac{\mathbf{U}^{(d)} - \mathbf{U}^n}{\Delta t} - \mathbf{RHS}^{n+1/2}\,, \tag{3}$$

where upper-case letters indicate quantities evaluated at Lagrangian coordinates. Obviously, the velocity in the particle domain $\mathcal{S}$ is simply given by the solid-body motion,

$$\mathbf{U}^{(d)}(\mathbf{X}) = \mathbf{u}_c + \boldsymbol{\omega}_c \times (\mathbf{X} - \mathbf{x}_c) \qquad \mathbf{X} \in \mathcal{S}\,, \tag{4}$$

as a function of the translational and rotational velocities of the particle, $\mathbf{u}_c$, $\boldsymbol{\omega}_c$, and its center coordinates, $\mathbf{x}_c$.

The final element of the method of [12] is the transfer of the velocity (and r.h.s. forces) from Eulerian to Lagrangian positions as well as the inverse transfer of the forcing term to the Eulerian grid positions. For this purpose we define a Cartesian grid $\mathbf{x}_{ijk}$ with uniform mesh width h in all three directions. Furthermore, we distribute so-called discrete Lagrangian force points $\mathbf{X}_l$ (with $1 \leq l \leq N_L$) evenly on the particle surface. Using the regularized delta function formalism of [14], the transfer can be written as:

$$\mathbf{U}(\mathbf{X}_l) \;=\; \sum_{ijk} \mathbf{u}(\mathbf{x}_{ijk})\, \delta_h(\mathbf{x}_{ijk} - \mathbf{X}_l)\, h^3\,, \tag{5a}$$

$$\mathbf{f}(\mathbf{x}_{ijk}) \;=\; \sum_{l} \mathbf{F}(\mathbf{X}_l)\, \delta_h(\mathbf{x}_{ijk} - \mathbf{X}_l)\, \Delta V_l\,, \tag{5b}$$

where ΔV_l designates the forcing volume assigned to the lth force point. We use the particular function δ_h given in [15] which has the properties of continuous differentiability, second order accuracy, support of three grid nodes in each direction and consistency with basic properties of the continuous delta function.

It should be underlined that the force points are distributed on the interface between fluid and solid, $\mathbf{X}_l \in \partial\mathcal{S}$, and not throughout the whole solid domain $\mathcal{S}$. The reason for this is efficiency: the particle-related work scales as $(D/h)^2$ instead of $(D/h)^3$.

The above method has been implemented in a staggered finite-difference context, involving central, second-order accurate spatial operators, an implicit treatment of the viscous terms and a three-step Runge-Kutta procedure for the non-linear part. Continuity in the entire domain is enforced by means of a projection method. For completeness, the full semi-discrete equations for each Runge-Kutta sub-step (indicated by superscript ^{k}) are given in the following (superscripts $^{(m)}$

refer to a particle in the range $1 \leq m \leq N_p$):

$$
\begin{aligned}
\tilde{\mathbf{u}} &= \mathbf{u}^{k-1} + \Delta t \left(2\alpha_k \nu \nabla^2 \mathbf{u}^{k-1} - 2\alpha_k \nabla p^{k-1} \right. \\
&\quad \left. -\gamma_k \left[(\mathbf{u}\cdot\nabla)\mathbf{u} \right]^{k-1} - \zeta_k \left[(\mathbf{u}\cdot\nabla)\mathbf{u} \right]^{k-2} \right) && \text{(6a)} \\
\tilde{U}_\beta(\mathbf{X}_l^{(m)}) &= \sum_{ijk} \tilde{u_\beta}(\mathbf{x}_{ijk})\, \delta_h(\mathbf{x}_{ijk} - \mathbf{X}_l^{(m)})\, h^3 \quad \forall\, l;\ m;\ 1 \leq \beta \leq 3 && \text{(6b)} \\
\mathbf{F}(\mathbf{X}_l^{(m)}) &= \frac{\mathbf{U}^{(d)}(\mathbf{X}_l^{(m)}) - \tilde{\mathbf{U}}(\mathbf{X}_l^{(m)})}{\Delta t} \qquad \forall\, l;\ m && \text{(6c)} \\
f_\beta(\mathbf{x}_{ijk}) &= \sum_{m=1}^{N_p} \sum_{l=1}^{N_L} F_\beta(\mathbf{X}_l^{(m)})\, \delta_h(\mathbf{x}_{ijk} - \mathbf{X}_l^{(m)})\, \Delta V_l^{(m)} \quad \forall\, i, j, k \\
&\qquad 1 \leq \beta \leq 3 && \text{(6d)} \\
\nabla^2 \mathbf{u}^* - \frac{\mathbf{u}^*}{\alpha_k \nu \Delta t} &= -\frac{1}{\nu \alpha_k} \left(\frac{\tilde{\mathbf{u}}}{\Delta t} + \mathbf{f}^k \right) + \nabla^2 \mathbf{u}^{k-1} && \text{(6e)} \\
\nabla^2 \phi^k &= \frac{\nabla \cdot \mathbf{u}^*}{2\alpha_k \Delta t}\,, && \text{(6f)} \\
\mathbf{u}^k &= \mathbf{u}^* - 2\alpha_k \Delta t \nabla \phi^k\,, && \text{(6g)} \\
p^k &= p^{k-1} + \phi^k - \alpha_k \Delta t\, \nu \nabla^2 \phi^k && \text{(6h)}
\end{aligned}
$$

where the set of coefficients α_k, γ_k, ζ_k ($1 \leq k \leq 3$) is given in [16]. The intermediate variable ϕ is the so-called "pseudo-pressure", $\mathbf{u}^*$ the predicted velocity field; both are discarded after each step.

The particle motion is determined by the Runge-Kutta-discretized Newton equations for rigid-body motion, which are weakly coupled to the fluid equations.

During the course of a simulation, particles can approach each other closely. However, very thin liquid inter-particle films cannot be resolved by a typical grid and therefore the correct build-up of repulsive pressure is not captured which in turn can lead to possible partial "overlap" of the particle positions in the numerical computation. In practice, various authors use artificial repulsion potentials which prevent such non-physical situations [17–19]. Here we apply the collision strategy of Glowinski et al. [20], relying upon a short-range repulsion force (with a range of $2\Delta x$). The stiffness parameter appearing in the definition of the repulsion force has been calibrated in simulations of two sedimenting particles and particle-wall interactions.

The current algorithm has been implemented for parallel machines with distributed memory, using the MPI library. For reasons of efficiency, the Helmholtz problems in (6e) are simplified by second-order-accurate approximate factorization and the Poisson problem in (6f) is solved by a multi-grid technique. We use a domain decomposition technique for distributing the Eulerian nodes over a three-dimensional processor grid. Each processor treats the particles currently located in its sub-domain. Additionally, the neighbor processors need to contribute to the transfer operations (6b, 6d) whenever particle domains happen to overlap sub-domains of the distributed grid. The particle treatment can therefore be described as a "master-and-slave" technique.

Our method has been subjected to a wide array of validation cases: (i) Taylor-Green flow in an immersed region; (ii) uniform flow around a stationary cylinder; (iii) uniform flow around an oscillating cylinder; (iv) a freely rotating circular disc in Couette flow; (v) a single sedimenting circular disc; (vi) a freely-rotating cylinder in Couette flow; (vii) drafting-kissing-tumbling of two circular discs; (viii) pure wake interaction of two circular discs; (ix) sedimentation of a single spherical particle; (x) pure wake-interaction of two spherical particles; (xi) drafting-kissing-tumbling of two spherical particles. Most of these simulations have been documented in [12, 21–24].

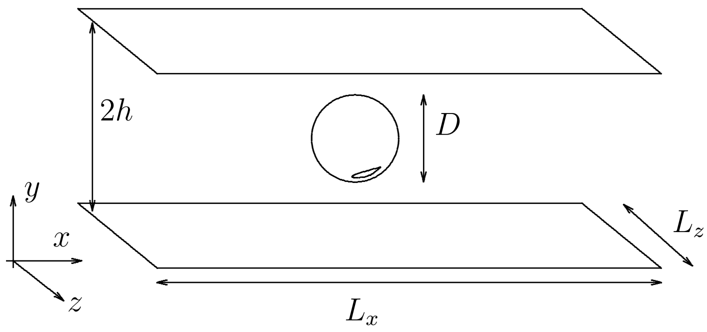

Figure 1: Schematic of the geometry for the case of a fixed sphere in plane channel flow.

case	Re_b	Re_D	$\bar{c}_D$	$\bar{c}_D$ (indirect)	c'_{Ly}	c'_{Lz}	St
15k	539.8	130.7	0.7211	0.7367	0	0	–
15f	851.8	206.3	0.5870		0.0713	0.0300	0.1311

Table 1: The forces acting upon a fixed sphere in a plane channel, expressed in terms of the dimensionless coefficients for drag and lift and the Strouhal number (for cases of periodic behavior). The Reynolds number Re_D is based upon the sphere diameter and the mean bulk velocity.

3 Results

3.1 A fixed single sphere in a periodic plane channel

Here we simulate plane channel flow with a spherical obstacle (cf. figure 1). We consider a bi-periodic domain of integration of size $\Omega = 2h \times 2h \times 2h$ and use a grid with $128 \times 128 \times 128$ uniformly-spaced nodes. The size of the sphere is $D/h = 0.2422$ which means that the diameter is resolved by 31 grid nodes. As a consequence, $N_L = 3019$ Lagrangian force points are located on the surface of the sphere. The time step is such that $CFL \approx 0.75$. Our simulations are run at constant mean streamwise pressure gradient $\mathrm{d}\bar{p}/\mathrm{d}x$ (where the overbar designates a time average). We have chosen a flow regime in which the flow without the obstacle is well below the threshold for turbulent flow (bulk flow Reynolds number below 1000). Two values for viscosity are chosen, one leading to stationary flow (case 15k) and one leading to time-periodic flow (case 15f).

The drag coefficient is obtained from the following definition of the streamwise force:

$$F_x = c_D \frac{1}{2} \rho_f U_b^2 A \,, \tag{7}$$

with $A = \pi(D/2)^2$, and similarly for the remaining components. F_x is obtained from the immersed boundary method as the sum of all fluid-solid coupling contributions (i.e. a sum over all Lagrangian points in relation 6c above). Another method is to compute the drag force from a streamwise momentum balance. For stationary flow, there is an equilibrium between the driving pressure gradient, the wall shear and the drag force, viz.

$$\partial_x p = \frac{\nu}{2h} \left((\partial_y u)_{y=2h} - (\partial_y u)_{y=0} \right) + \frac{F_x}{2h L_x L_z} \,, \tag{8}$$

We have checked that both methods gave consistent values of F_x to within 2% (case 15k). Small differences are expected due to the fact that the direct evaluation is done for the force imposed during the predictor step, which is later corrected in the projection step. The ability to evaluate the hydrodynamic forces acting upon a sphere accurately and efficiently is of considerable importance in particulate flow since this procedure needs to be repeated for each particle at each time step in order to drive the Newton equation for particle acceleration.

The Strouhal number is defined as:

$$St = \frac{f_{lift-y} D}{U_b} , \tag{9}$$

where f_{lift-y} is the frequency of the oscillations of the lift forces in the wall-normal direction. This frequency has been determined by Fourier analysis of a time sequence of F_y which shows a single pronounced peak.

The bulk Reynolds number of the channel flow is defined as:

$$Re_b = \frac{U_b h}{\nu} . \tag{10}$$

The Reynolds number corresponding to the flow around the sphere is defined as follows:

$$Re_D = \frac{U_b D}{\nu} . \tag{11}$$

Table 1 gives the values for the Reynolds numbers and the resulting drag/lift coefficients as well as the value for the Strouhal number.

Comparing our present results with simulations performed by Stoesser using the code MGLET we observe a difference in drag of 1.54% (case 15k), using the indirect method of evaluation. It should be mentioned that the time step for the computations is quite different, with MGLET running at 8 times smaller steps.

Figure 5 shows the time evolution of the bulk velocity in our simulations. In case 15k, a steady state is reached rapidly where the flow field is stationary. In case 15f (with a sphere Reynolds number slightly above 200), the transient is longer, leading to a periodic flow. Also included is the time history of a case (15l) with an intermediate viscosity, where the flow asymptotically approaches a stationary state.

Figure 6 shows the time history of forces acting on the sphere in the periodic case 15f. It can be seen that the two force components in the cross-stream direction correspond to sinusoidal signals with different frequencies, whereas the drag component obviously contains more than one mode. From the plot in frequency space (cf. figure 7) we deduce that indeed the drag evolution corresponds to a superposition of two dominant frequencies, each one corresponding to approximately twice the value of one of the modes of the lift components. Those, in turn, have a frequency ratio of approximately 1.5, with the spanwise oscillation being faster. In figure 8 we show the drag and lift variations in phase space. The curve for drag vs. wall-normal lift exhibits an 8-shaped pattern which does not quite collapse for subsequent periods. On the other hand, the behavior of the wall-normal vs. the spanwise lift is characterized by a more complicated multi-loop pattern, which, in time, seems to fill up the whole plane bounded by the maximum values of the oscillations. This latter evolution is apparently due to the non-integer value of the frequency ratio.

Figure 9 shows the flow fields of cases 15k and 15f, visualized by means of the λ_2 criterion of [25]. These plots and additional animations of the flow (not shown) give an impression of how the differences between the lift components in the two cross-stream directions are caused by the alternating shedding mechanism in the wake.

A comparison of our results with those obtained by Stoesser with MGLET is shown in figure 10 for the stationary case 15k. An excellent match for profiles of the different velocity components taken at various positions in the domain can be observed.

3.2 Turbulent flow in a plane half-channel

For the simulation of turbulent flow in a plane channel bounded by one solid wall and one slip wall we use the following boundary conditions for velocity:

$$y = 0 : \quad \mathbf{u} = 0 , \qquad y = h : \quad \mathbf{u} \cdot \mathbf{n} = 0 , \; \frac{\partial(\mathbf{u} - \mathbf{u} \cdot \mathbf{n})}{\partial \mathbf{n}} = 0 \tag{12}$$

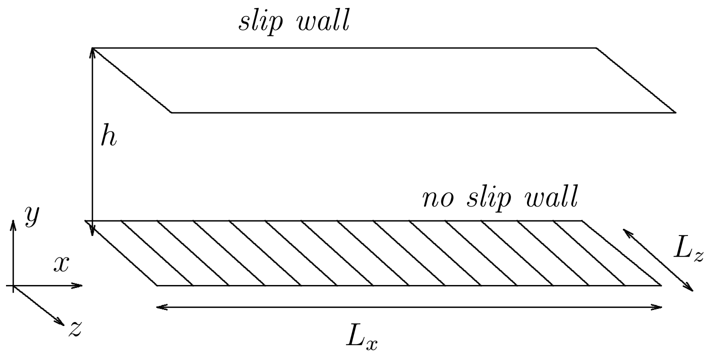

Figure 2: Schematic of the geometry for the case of turbulent flow in a plane half-channel.

case	Re_b	Re_τ	D/h	$D/\Delta x$	N_L	D^+	Δx^+	y_0	A	$t_{stat} u_b/h$
13	2700	445.8	0.2422	62	12076	108.0	1.74	0.210	−2.5	59.2
16	2700	224.5	0.0547	14	616	12.3	0.88	0.035	−0.5	56.9

Table 2: Parameters and results of the simulation of turbulent flow over a rough wall. Note that the bulk Reynolds number is defined as $Re_b = U_b(h - D)/\nu$.

along with $\partial p/\partial \mathbf{n} = 0$ on both walls. The flow is periodic in the x- and z-directions (cf. figure 2).

In order to validate our implementation of this type of configuration (which had previously not been considered in SUSPENSE) we have carried out simulations of low-Reynolds number flow in a small domain. The computation was initialized with a field obtained from a fully spectral code run for the full channel at the same streamwise and spanwise dimension; the field was then spectrally interpolated upon the present grid.

During the following simulation it was checked that the correct behavior at the boundaries was observed and that turbulence could indeed be maintained. The integration time was not sufficient in order to accumulate significant statistics.

3.3 Flow over an array of wall-mounted spheres (roughness)

Here we introduce fixed spheres near the solid wall of the plane half-channel configuration of § 3.2. Figure 3 shows the geometry in the two particular cases which we have simulated. Two layers of spheres (with diameter $D/h = 0.2422$ in case 13 and $D/h = 0.0547$ in case 16) are located at the lower boundary: the first just above the solid wall and the other one underneath it such that only a small fraction protrudes into the fluid domain. This second layer is arranged in a staggered manner with respect to the top layer, and, therefore, it will prevent that the top layer will simply "roll away" in the subsequent case with mobile particles.

The bi-periodic box measures $\Omega = 1.5h \times 1h \times 0.75h$, resolved by a grid with $384 \times 256 \times 192$ nodes. The time step is such that $CFL \approx 0.75$. Table 2 shows all the relevant parameters as well as the results of the runs which will be discussed below. These simulations were run at a constant volume flow rate with $Re_b = 2700$ (the value of reference [26]). Please note that in the case with the roughness elements of larger diameter (case 13), the turbulence intensity increased to such a degree that the grid size in wall units is approximately twice as large as initially planned. Therefore, in further runs with the configuration of case 13, the viscosity should be increased.

The streamwise momentum, averaged in time and over wall-parallel planes and integrated over

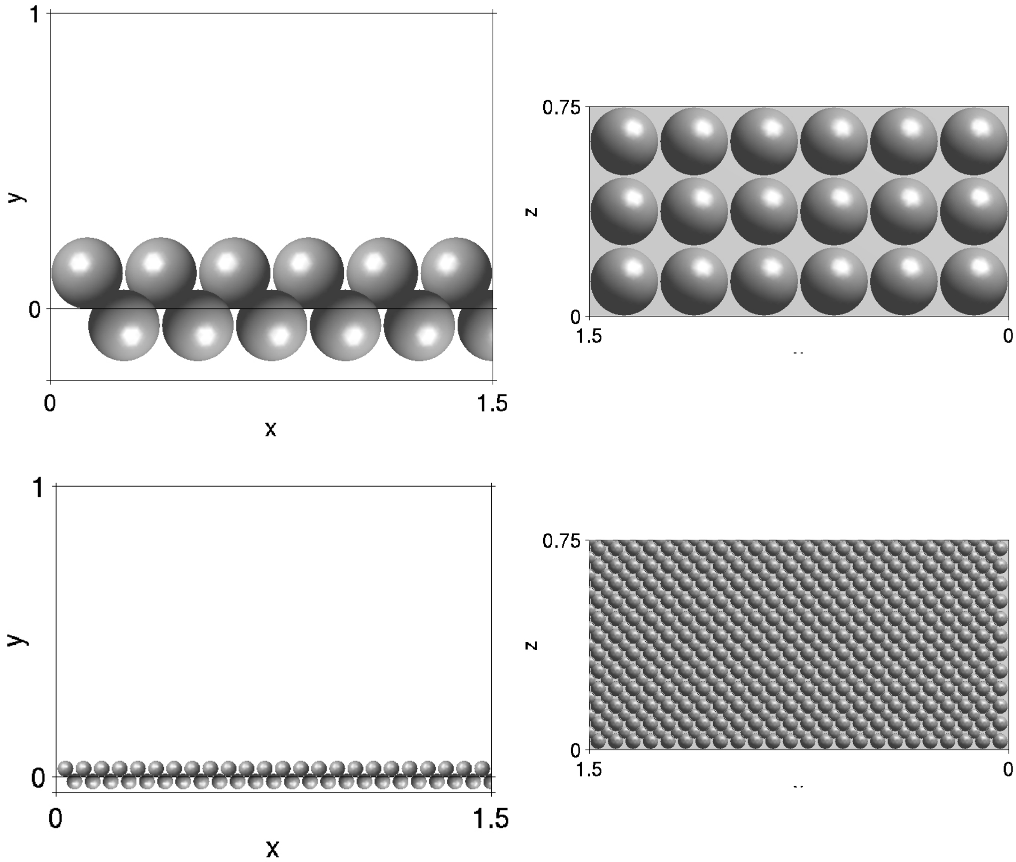

Figure 3: Flow geometry of cases 13 (top row) and 16 (bottom row).

the channel-height reads:

$$\partial_x \langle p \rangle \, h = \underbrace{-\nu (\partial_y \langle u \rangle)_{y=0} + \sum_{i=1}^{N_p^{fixed}} \int_0^h \langle F_x^{(i)} \rangle \mathrm{d}y}_{= -\tau_w = -u_\tau^2} \,, \tag{13}$$

where the sum runs over all fixed particles and $F_x^{(i)}$ is the sum of all solid-fluid coupling force contributions of the ith particle in the x-direction (cf. 6c). Note that $\langle \cdot \rangle$ means average over time and planes parallel to the wall and that normalization in wall units is indicated by the familiar superscript $^+$. In equation (13) we associate the right-hand-side with the wall shear τ_w which is equal to the sum of the viscous drag on the wall and the total drag (i.e. viscous and pressure-induced) on the spheres (cf. [7]). Figure 11 shows the time evolution of the wall shear. The time-average lets us compute a value for the friction velocity and Re_τ (cf. table 2).

Figure 12 depicts the mean profiles of the total shear stress $\tau_{tot} = \langle u'v' \rangle - \nu \partial_y \langle u \rangle$ after accumulation of $t_{stat} u_b / h = 59.2$ (56.9) in case 13 (16). Since the variation does not follow a straight line (as it should for wall distances above the top layer of roughness elements), we conclude that our statistics are not fully converged. Judging by the shape of the profile, we estimate that additional statistics need to be accumulated over a period of $30h/u_b$ to $50h/u_b$.

Plots in figure 13 show the first and second moments of velocity from our preliminary statistics. Note that we should obtain a logarithmic region of the form:

$$\frac{\langle u \rangle}{u_\tau} = \frac{1}{\kappa} \log \left(\frac{(y - y_0) u_\tau}{\nu} \right) + A \tag{14}$$

which means that, given a data-set for $\langle u \rangle = f(y)$, we have in principle 4 unknowns: u_τ, κ, y_0 and A. Here we will assume the standard value for the slope ($\kappa = 0.41$) and use u_τ as defined in (13) and determined from figure 11. Concerning the offset of the origin, y_0, it will lie in the range $0 \leq y_0 \leq D$ [7]. Using a visual fit of the statistics accumulated so far, wed obtain the values for y_0 and A shown in table 2; the graph of the logarithmic law is given in figure 13. The logarithmic fit in case 13 is obviously better; at this stage, the mean velocity in case 16 still exhibits a "bump" near the surface. Clearly, more samples are needed. However, we can already note that the procedure is adequate for the purpose of determining a reference value for u_τ which will be used mainly for normalizing the results below.

Histograms for the three force components acting upon the top layer of spheres in the two simulations are shown in figure 14 in terms of the coefficients c_D, c_{Ly}, c_{Lz} defined as in equation (7). The curve for the spanwise component is symmetric with respect to the origin, as expected. Both lift and drag show a bias towards positive values, i.e. forces which would tend to induce forward and upward motion in free particles.

It is interesting to compare these forces with those necessary to induce actual particle motion would the particles be free. First, we compare the statistics of the lift force with the gravitational force acting upon the particles used in the simulations of § 3.4 below (figure 16). It is obvious that lift-off from rest is not possible for the two highest gravitational forces in case 13 and for the four highest in case 16.

As will be seen below in the simulations with free particles, however, erosion is initiated not by vertical motion but by particle motion following the surface of the fixed bed. This means that we need to consider the forces acting in the tangential direction at the contact point between the two layers of spheres. The projection of this direction into the (x,y)-plane forms an angle $\alpha = 35.3°$ with the horizontal (in both cases 13 and 16). The resulting force in this direction then reads (cf. schematic in figure 4):

$$F_t = -G \sin(\alpha) + F_x \cos(\alpha) + F_y \sin(\alpha) \,. \tag{15}$$

The histogram in figure 16 shows the sum of the drag and lift contributions to (15) and compares it to the gravitational contribution for the different particles used in § 3.4. In all cases, sufficiently

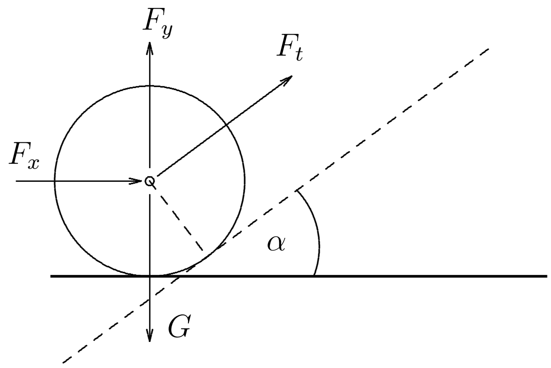

Figure 4: Schematic of the forces acting upon a particle in the (x,y)-plane and the resulting force F_t in the direction which forms an angle α with the horizontal plane.

strong hydrodynamical forces occur in order to overcome the gravitational force projected upon the sloped line. This would suggest that particle motion can be initiated in all those cases. However, two additional points should be considered:

- The force balance in (15) does not take into account frictional forces during particle contact. This would tend to delay the onset of particle motion. However, the simulations below do not consider this phenomenon either, as it is currently outside the scope of our study.
- The histogram for the force balance is evaluated for individual spheres in the top layer as if they were isolated from their neighbors in that layer. In reality, particle motion in the tangential direction can only take place when a group of particles moves at the same time, since particles aligned in the streamwise direction are blocking each other. This basically means that the force balance needs to be evaluated collectively for a streamwise "row" of particles in order to obtain a meaningful histogram. Figure 17 shows the result when averaging the data over such rows. It can be seen that the number of events which have the potential to overcome the gravitational force in the tangential direction collectively is smaller than indicated by the individual evaluation. The plots in this figure show that only the heaviest spheres in both configurations would not be set into motion. We will see in § 3.4 that this is the case in the dynamical simulation (i.e. particles move in all cases except for 13e and 16d; cf. table 3).

3.4 The onset of erosion

The configuration is the same as in § 3.3, except that the top layer of spheres (those which have their center located at $y = D/2$) is not fixed. The initial field is taken from the simulation with fixed spheres at a time where the flow is considered fully developed. The simulations are then run for a certain time interval, say t_{obs}. In the case of an observed particle motion, the simulation can be terminated; conversely, some upper bound for t_{obs} needs to be set in practice beyond which erosion is not expected to take place any more (or if it would do so, would be considered marginal anyway). Note that this time interval depends on the size of the box which is used, since the latter determines the number of potential turbulent "events" which take place in the numerical experiment in a given interval. This point will be further discussed in § 4.

For each of the two geometrical configurations, the value of the gravity is varied for a fixed density ratio $\rho_p/\rho_f = 1.25$. Thereby we can explore the bounds for the onset of erosion. The set of values for $|\mathbf{g}|$ is given in table 3. The table also indicates whether erosion was observed in a particular simulation. It can be seen that erosion takes places in all cases except for cases 13e and 16d. This result is consistent with our previous prediction based upon the force balance acting

case	D/h	ρ_p/ρ_f	$|\mathbf{g}|$	u_∞	$t_{obs}u_b/h$	erosion?
13c	0.2422	1.25	0.15	0.130		y
13d	0.2422	1.25	0.20	0.160		y
13f	0.2422	1.25	0.30	0.213		y
13e	0.2422	1.25	0.40	0.262	16.9	n
16c	0.0547	1.25	0.20	0.026		y
16g	0.0547	1.25	0.40	0.043		y
16f	0.0547	1.25	0.60	0.058		y
16e	0.0547	1.25	0.80	0.071		y
16d	0.0547	1.25	1.00	0.083	22.2	n

Table 3: Parameters for the simulation of sediment erosion. The terminal velocity is evaluated according to appendix A.

upon fixed particles and the geometrical constraints imposed by the specific shape of the bed (i.e. the arrangement of the lower layer of spheres).

Figures 18-19 show a sequence of particle positions in cases 13d and 16c. In both of these cases erosion is observed. The visualizations show that at first, a whole "row" of particles is fluidized and moves coherently in the streamwise direction at a small wall-distance. At a later stage, the chain of particles becomes distorted and individual particles get lifted out of the configuration and get carried away by faster fluid at larger wall-distances. Other particles follow and the whole configuration gets highly disordered.

In case 16c (figure 19) we clearly observe a large scale structure of the particle configuration. The rows of particles in the center of the channel are not fluidized and lift-off takes place only near the (periodic) lateral boundary. This kind of behavior was observed in all the cases of series 16, where erosion took place. It appears to be directly related to the coherent flow structures of the carrier phase, as shown in figure 20. Here we see a snapshot of the flow field at the onset of erosion of case 16f, visualized by means of isosurfaces corresponding to locally high/low relative velocities and to intense vortex structures. It can be observed that the lateral locations where particle fluidization takes place coincide with the presence of the high-velocity streak which is correlated nearly over the full channel period. Further analysis of sequences of flow fields during the early stages of erosion will be performed in the future.

Results of parametrical studies for observed/not observed erosion are often plotted in either one of the following two representations: τ_w^* vs. D^+ or u_τ/u_∞ vs. D^+, where τ_w^* is a dimensionless shear stress defined as

$$\tau_w^* \quad = \quad \frac{u_\tau^2}{|\mathbf{g}|D(\frac{\rho_p}{\rho_f}-1)} \,. \tag{16a}$$

On the other hand, the terminal velocity of a particle u_∞ can be computed from the balance between drag force and gravitational force:

$$u_\infty^2 = \left(\frac{\rho_p}{\rho_f}-1\right) D|\mathbf{g}|\frac{4}{3}\frac{1}{c_D} \,, \tag{17}$$

which means that τ_w^* can be expressed in terms of the terminal velocity as follows:

$$\tau_w^* = \frac{u_\tau^2}{u_\infty^2}\frac{4}{3c_D} \,. \tag{18}$$

Consequently, the two ways of presenting the onset of erosion are in reality closely related, the difference being principally the drag coefficient which appears in the definition of the terminal velocity. It should be stressed that this is the drag coefficient at equilibrium, i.e. when the particle has already reached its terminal velocity in ambient conditions or in a uniform flow field. However, it is difficult to see how this quantity should be decisive in determining the erosion of a particle lifting off from rest, since this is an entirely different dynamical process. It seems that the terminal velocity would rather play a role in the sedimentation and deposition process than in the opposite mechanism of resuspension.

In figures 21-22, our present results are compared to experimental observations of erosion reported in reference [5]. Therein two series of experiments were conducted in a water channel ($Re_b = 5000 \ldots 35000$), one for erosion of particles on a smooth wall and one for sediment placed on a rough wall. In the latter case, the ratio of particle diameter to the size of the roughness elements D_r/D ranged from 0.07 to 1 which led to significant hiding effects. We recall that the protrusion height of the roughness elements in our present arrangement is significantly smaller ($D/D_r = 4.35, 3.25$), which means that our particles experience a much smaller hiding effect.

Concerning the visualization of the results in terms of the dimensionless shear stress τ_w^* in figures 21-22, we observe that our data implies a critical value which increases from the smaller particle size in series 16 ($\tau_w^* \gtrapprox 0.12$) to the larger particles in series 13 ($\tau_w^* \gtrapprox 0.2$). This behavior is consistent with the "dip" in the classical Shields curve which is found around $D^+ = 10$. It can be speculated that the lower threshold at this length scale might be related to the scaling properties of the coherent structures in the near-wall region. This lead shall be further explored in future studies.

The threshold for the onset of erosion observed in our simulations is somehow in between the values of the two data sets of reference [5]. Compared with the trend of the experimental data for smooth walls (figure 21), the onset of erosion happens for slightly higher values in our simulations. The opposite is true when comparing our data to the measurements taken on a rough bed (figure 22). This result is consistent with the fact that our configuration can be considered as rough, albeit with a much smaller ratio of particle size to roughness height. However, it should be underlined that the comparison can only be of a qualitative manner since it is not possible to reproduce the conditions of the experiment exactly in the simulations.

Now turning to the comparison of the results plotted in terms of the ratio of friction velocity to terminal particle velocity u_τ/u_∞ in the same figures, we observe a large mismatch with respect to the experimental values, irrespective of the type of bed used therein. The trend here is that the critical ratio for erosion diminishes with the particle size. However, the slope is different from the experiments and there is a considerable vertical offset. Again, we remark that it is felt that this quantity is not an adequate indicator for the onset of erosion.

4 Conclusion

4.1 Summary and discussion

We have compared results of our present method with an independent implementation of a similar immersed boundary technique in the case of a single fixed sphere in laminar plane channel flow. The agreement was found to be generally very good.

We have simulated turbulent flow over a rough wall formed by a closely packed two-layer bed of spheres (with diameters equal to 12 and 108 wall units) at a bulk Reynolds number of 2700. Fully converged flow statistics were not accumulated. However, the simulations have provided important information about the forces acting on the roughness elements. The projection of these forces upon the tangential direction at the contact point between the two layers of spheres needs to be larger than the corresponding gravitational component, in order to be able to initiate particle motion along the surface. We have used histograms of these forces accumulated in our simulations for evaluating the probability of such motion; the result matches the outcome of our simulations involving freely moving sediment particles.

We have performed direct numerical simulations where the top layer of spheres of the roughness cases can translate and rotate freely (according to the balance of hydrodynamic and gravitational forces). By varying the value of gravitational acceleration (with fixed density) we have determined critical values for the onset of motion of heavy particles. It has been observed that the motion is initiated collectively by streamwise trains of particles which get perturbed at a later stage, followed by full entrainment of individual spheres into the flow. It was also observed for the smaller particles that the resuspension process correlates highly with the presence of areas with high values of wall shear beneath high-speed streaks.

Further, we have observed that the critical non-dimensional shear stress increases with the particle diameter, which could be taken as an indication that the ratio of sediment size to the size of characteristic coherent structures in the near-wall layer leads to a kind of selectivity. Under this hypothesis, it would not be possible for those structures to set very large particles into motion, and, consequently, those large particles would require a sufficiently strong mean flow, leading to a higher threshold value for erosion.

Expressed in parameter space, our results for the onset of erosion are not inconsistent with experimental observations of Niño et al. [5], considering the difficulty in reproducing similar conditions in our DNS. Some differences with respect to laboratory experiments of erosion are:

- Size of the periodic domain. One consequence of the relatively small box used herein is the absence of the largest structures in the logarithmic and outer layers of the boundary layer [27]. This means that some potentially important mechanisms for resuspension are not represented in our DNS. Moreover, the rather small streamwise length of the computational box means that flow structures are often fully correlated in this direction, which facilitates the onset of motion of trains of particles.

- Frictional forces. We have fully neglected all frictional contact forces between particles. However, friction would tend to hinder the onset of motion.

- Particle configuration. Particles in our simulation are densely packed and exactly staggered with respect to the layer below. In most experiments the conditions are not equally uniform, nor are they fully documented.

- Flow Reynolds number. The Reynolds number of our DNS is lower than in most experiments. It is not clear whether there is a sensitivity of the Shields diagram w.r.t this parameter.

4.2 Perspectives

Further analysis of the data generated up to this point will be particularly targeted at the mechanisms responsible for the entrainment of individual particles into the bulk flow once a train of particles is in motion along the surface.

The most immediate continuation of this work will then be the verification of our results in simulations with much larger domains of integration, in order to address the issue of decorrelation and to investigate the possible influence of large scale structures upon the process of resuspension. It will also be checked whether the observed mechanism of erosion is robust with respect to perturbations of the initial bed configuration.

In a next step we plan to study possible implementations for tangential contact forces in our formulation. This additional feature will help to assess the importance of friction in the process of erosion.

Acknowledgements

Fruitful discussions during the collaboration with J. Fröhlich and T. Stoesser are gratefully acknowledged. The computations were carried out at CIEMAT and HLRS. Travel expenses and computing time at HLRS were funded by the European Comission in the framework of the HPC-Europa project (grant RII3-CT-2003-506079). The author is grateful for the hospitality of the *Institut für Hydromechanik* (U. Karlsruhe).

References

[1] R. Jackson. *The dynamics of fluidized particles.* Cambridge U. Press, 2000.

[2] D. Kaftori, G. Hetsroni, and S. Banerjee. Particle behaviour in the turbulent boundary layer. I. Motion, deposition and entrainment. *Phys. Fluids*, 7(5):1095–1106, 1995.

[3] D. Kaftori, G. Hetsroni, and S. Banerjee. Particle behaviour in the turbulent boundary layer. II. Velocity and distribution profiles. *Phys. Fluids*, 7(5):1107–1121, 1995.

[4] Y. Niño and M.H. Garcia. Experiments on particle-turbulence interactions in the near-wall region of an open channel flow: implications for sediment transport. *J. Fluid Mech.*, 326:285–319, 1996.

[5] Y. Niño, F. Lopez, and M. Garcia. Threshold for particle entrainment into suspension. *Sedimentology*, 50:247–263, 2003.

[6] K.T. Kiger and C. Pan. Suspension and turbulence modification effects of solid particulates on a horizontal turbulent channel flow. *J. Turbulence*, 3(19):1–17, 2002.

[7] S. Leonardi, P. Orlandi, R.J. Smalley, L. Djenidi, and R.A. Antonia. Direct numerical simulations of turbulent channel flow with transverse square bars on one wall. *J. Fluid Mech.*, 491:229–238, 2003.

[8] L. Zeng, S. Balachandar, and P. Fischer. Wall-induced forces on a rigid sphere at finite Reynolds numbers. *J. Fluid Mech.*, 536:1–25, 2005.

[9] N.A. Patankar, P.Y. Huang, T. Ko, and D.D. Joseph. Lift-off of a single particle in Newtonian and viscoelastic fluids by direct numerical simulation. *J. Fluid Mech.*, 438:67–100, 2001.

[10] H.G. Choi and D.D. Joseph. Fluidization by lift of 300 circular particles in plane Poiseuille flow by direct numerical simulation. *J. Fluid Mech.*, 438:101–128, 2001.

[11] Y. Pan and S. Banerjee. Numerical investigation of the effects of large particles on wall-turbulence. *Phys. Fluids*, 9(12):3786–3807, 1997.

[12] M. Uhlmann. An immersed boundary method with direct forcing for the simulation of particulate flows. *J. Comput. Phys.*, 209(2):448–476, 2005.

[13] E.A. Fadlun, R. Verzicco, P. Orlandi, and J. Mohd-Yusof. Combined immersed-boundary finite-difference methods for three-dimensional complex flow simulations. *J. Comput. Phys.*, 161:35–60, 2000.

[14] C.S. Peskin. The immersed boundary method. *Acta Numerica*, 11:479–517, 2002.

[15] A.M. Roma, C.S. Peskin, and M.J. Berger. An adaptive version of the immersed boundary method. *J. Comput. Phys.*, 153:509–534, 1999.

[16] M.M. Rai and P. Moin. Direct simulation of turbulent flow using finite-difference schemes. *J. Comput. Phys.*, 96:15–53, 1991.

[17] K. Höfler and S. Schwarzer. Navier-Stokes simulation with constraint forces: Finite-difference method for particle-laden flows and complex geometries. *Phys. Rev. E*, 61(6):7146–7160, 2000.

[18] H.H. Hu, N.A. Patankar, and N.Y. Zhu. Direct numerical simulation of fluid-solid systems using the arbitrary Lagrangian Eulerian technique. *J. Comput. Phys.*, 169:427–462, 2001.

[19] R. Glowinski, T.W. Pan, T.I. Hesla, D.D. Joseph, and J. Périaux. A ficticious domain approach to the direct numerical simulation of incompressible viscous flow past moving rigid bodies: Application to particulate flow. *J. Comput. Phys.*, 169:363–426, 2001.

[20] R. Glowinski, T.-W. Pan, T.I. Hesla, and D.D. Joseph. A distributed Lagrange multiplier/fictitious domain method for particulate flows. *Int. J. Multiphase Flow*, 25:755–794, 1999.

[21] M. Uhlmann. New results on the simulation of particulate flows. Technical Report No. 1038, CIEMAT, Madrid, Spain, 2004. ISSN 1135-9420.

[22] M. Uhlmann. Numerical simulation of particulate flows: comparison of fictitious domain methods with direct and indirect forcing. In H.I. Andersson and P.-A. Krogstad, editors, *Advances in Turbulence X*, Proc. 10th Eur. Turb. Conf., pages 415–418, Trondheim, Norway, 2004.

[23] M. Uhlmann and A. Pinelli. Performance of various fluid-solid coupling methods for DNS of particulate flow. In S. Balachandar and A. Prosperetti, editors, *Computational approaches to disperse multiphase flow.* Kluwer *(in press)*, 2006.

[24] M. Uhlmann. An improved fluid-solid coupling method for DNS of particulate flow on a fixed mesh. In M. Sommerfeld, editor, *Proc. 11th Workshop Two-Phase Flow Predictions*, Merseburg, Germany, 2005. Universität Halle. ISBN 3-86010-767-4.

[25] J. Jeong, F. Hussain, W. Schoppa, and J. Kim. Coherent structures near the wall in a turbulent channel flow. *J. Fluid Mech.*, 332:185–214, 1997.

[26] J. Kim, P. Moin, and R. Moser. Turbulence statistics in a fully developed channel flow at low Reynolds number. *J. Fluid Mech.*, 177:133–166, 1987.

[27] J. Jiménez. The largest scales of turbulent wall flows. *CTR Res. Briefs*, pages 137–154, 1998.

[28] H. Schlichting. *Boundary-Layer Theory.* McGraw-Hill, seventh edition, 1979.

A Determination of the terminal particle velocity

We evaluate the terminal velocity u_∞ for our different particles by integrating the following equation of vertical particle motion until convergence ($\dot{u}_c = 0$):

$$\dot{u}_c = u_c^2 \frac{\rho_f}{\rho_p} \frac{3}{4D} c_D(Re_D) + \left(1 - \frac{\rho_f}{\rho_p}\right) |\mathbf{g}| \,, \tag{19}$$

where the standard correlations for the drag coefficient are used [28]:

$$c_D = \begin{cases} \dfrac{24}{Re_D} & Re_D < 2 \,, \\ \dfrac{18.5}{Re_D^{0.6}} & Re_D < 500 \,, \\ 0.44 & Re_D < 2 \cdot 10^5 \,. \end{cases} \tag{20}$$

The resulting values for u_∞ are given in table 3. In reference [5] a slightly different expression for the drag was used. However, it was checked that the difference does not play a significant role.

Figures

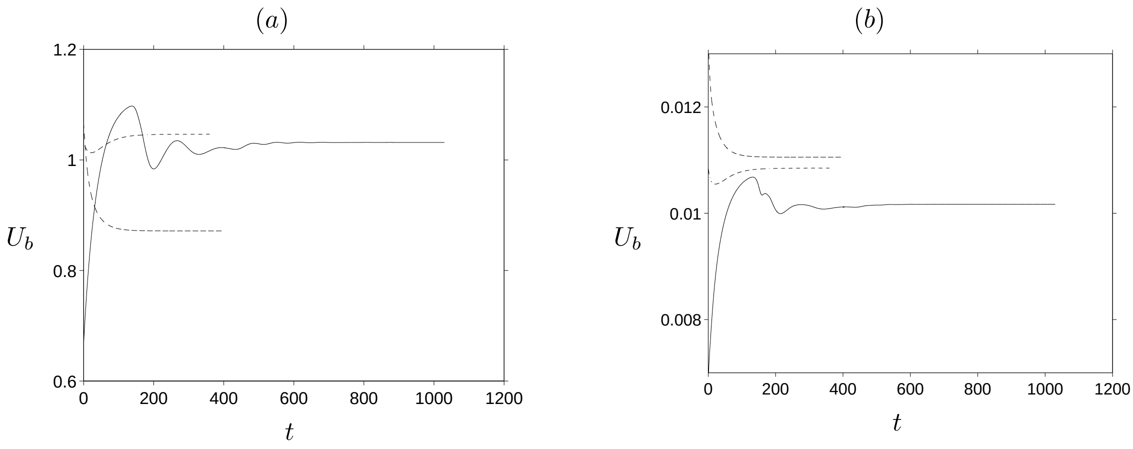

Figure 5: Convergence of the bulk velocity (a) and wall-gradient of velocity (b) in the case of a single sphere in plane channel flow, driven at constant pressure gradient. ---- , case 15k, —·— , case 15l, ——— , case 15f.

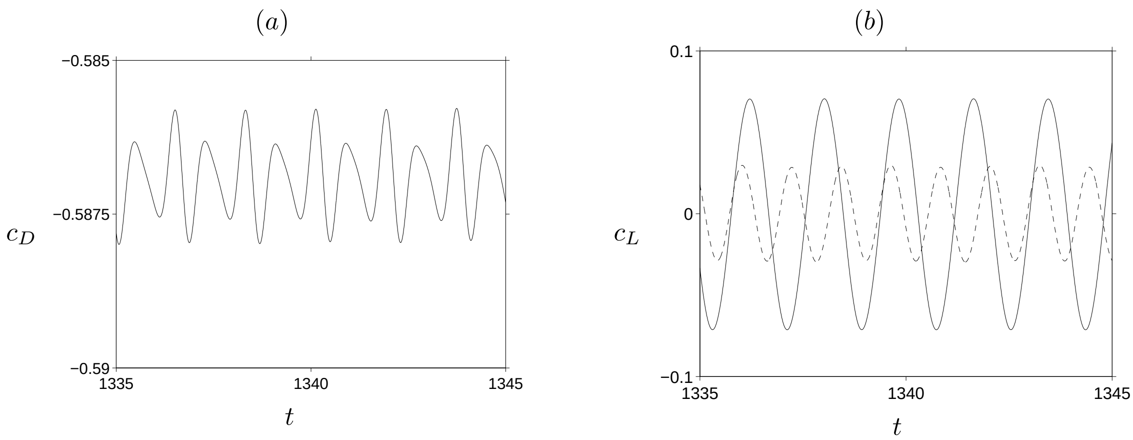

Figure 6: Forces acting upon a single sphere in a plane channel in case 15f (time-periodic flow). (a) drag; (b) the two components of the lift: ——— , c_{Ly}, ---- , c_{Lz}.

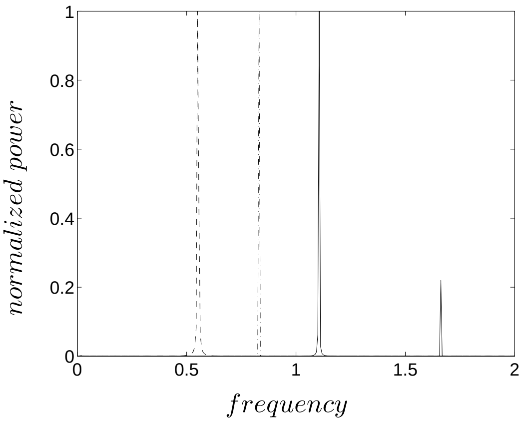

Figure 7: Frequency spectrum of time series of the hydrodynamical forces shown in figure 6. ——— , c_d; - - - - , c_{Ly}, —·— , c_{Lz}.

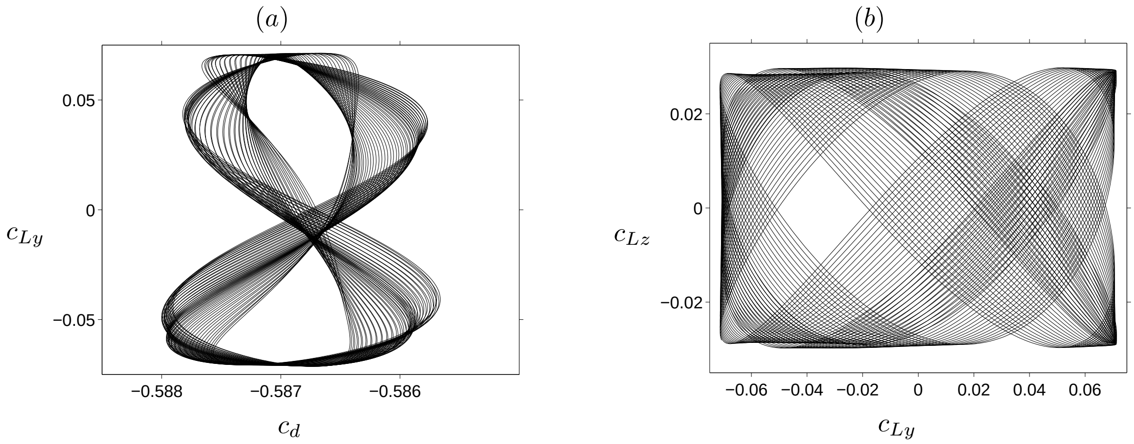

Figure 8: Phase-space diagrams of the temporal evolution of (a) wall-normal lift vs. drag and (b) spanwise vs. wall-normal lift of the periodic case 15f for an interval of 110 time units.

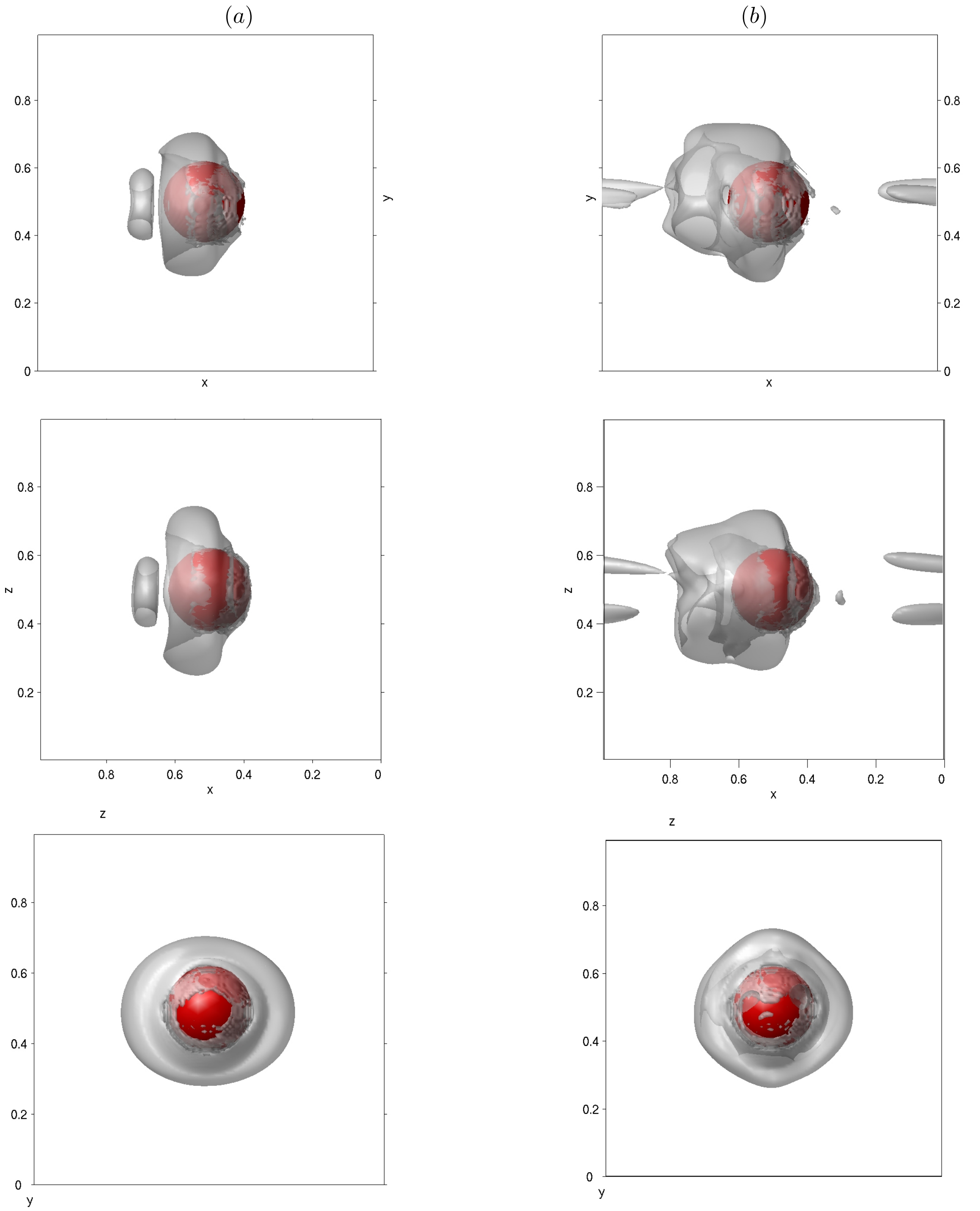

Figure 9: Flow field around a single sphere in a plane channel. (a) case 15k (stationary flow); (b) case 15f (time-periodic flow; a snapshot is shown). The gray surface shows vortical structures by means of isovalues of the λ_2 criterion [25]. The top row shows a view looking in the z-direction, the center row in y and the bottom row in x.

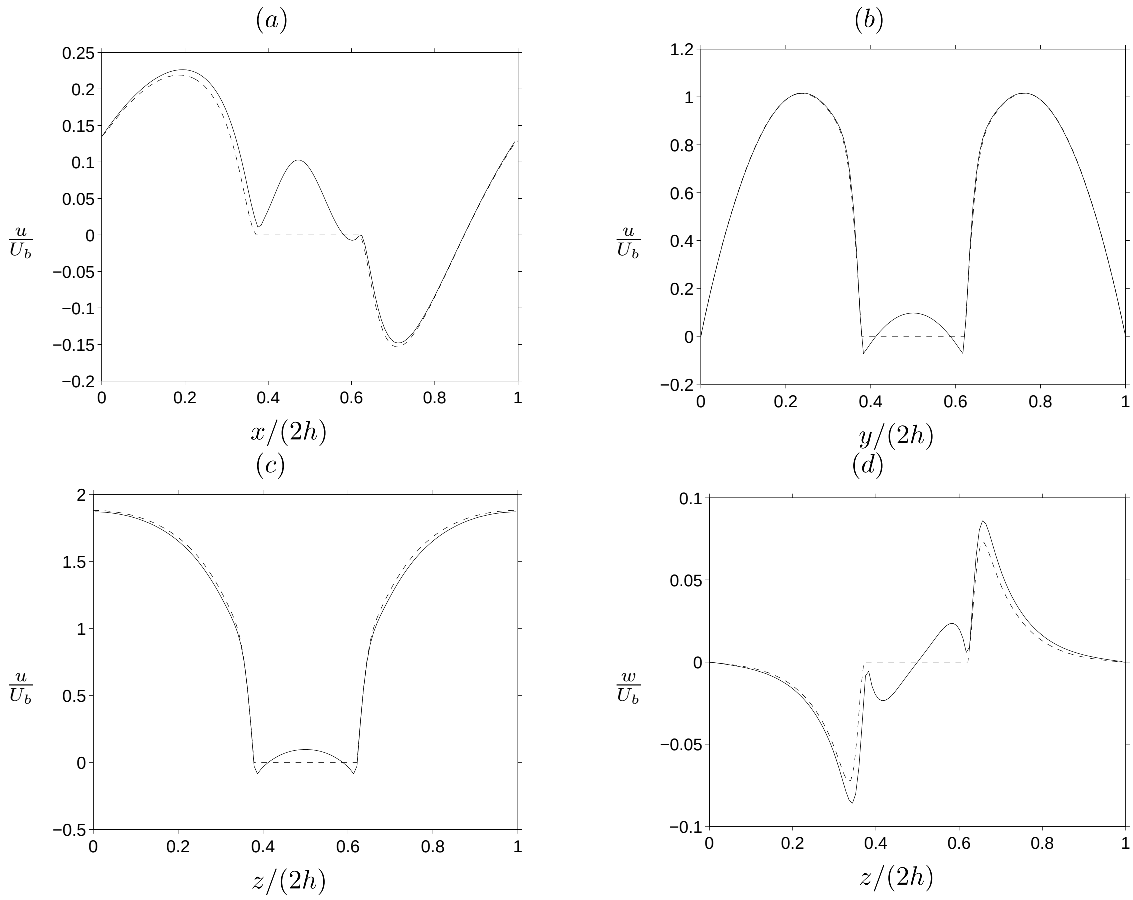

Figure 10: Profiles of the streamwise and spanwise velocity for case 15k (stationary flow), comparing present results (———) with those obtained by Stoesser, using the code MGLET (- - - -). The data is sampled at: (a) $y = z = 0.5$; (b) $x = z = 0.5$; (c) $x = y = 0.5$; (d) $x = y = 0.5$.

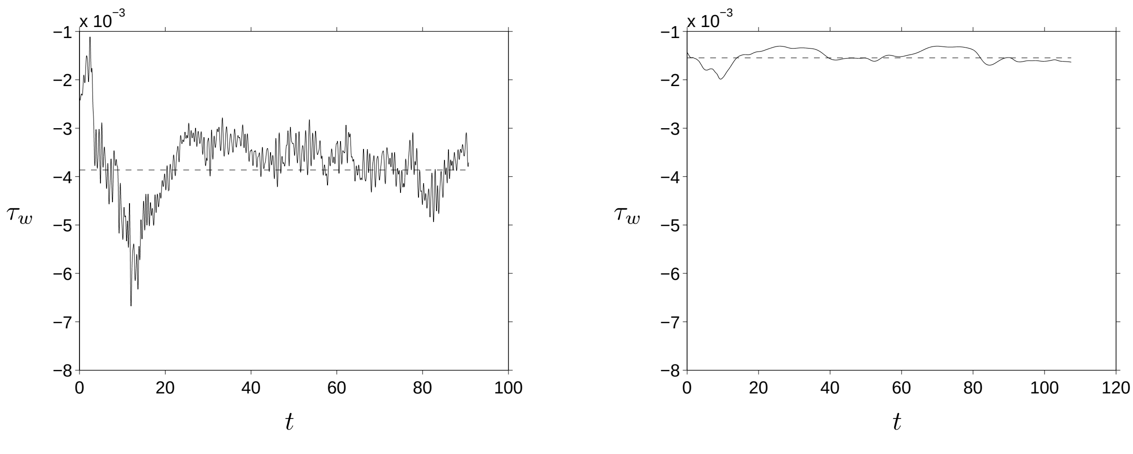

Figure 11: Time evolution of the plane-averaged wall shear in case 13 (left) and case 16 (right).

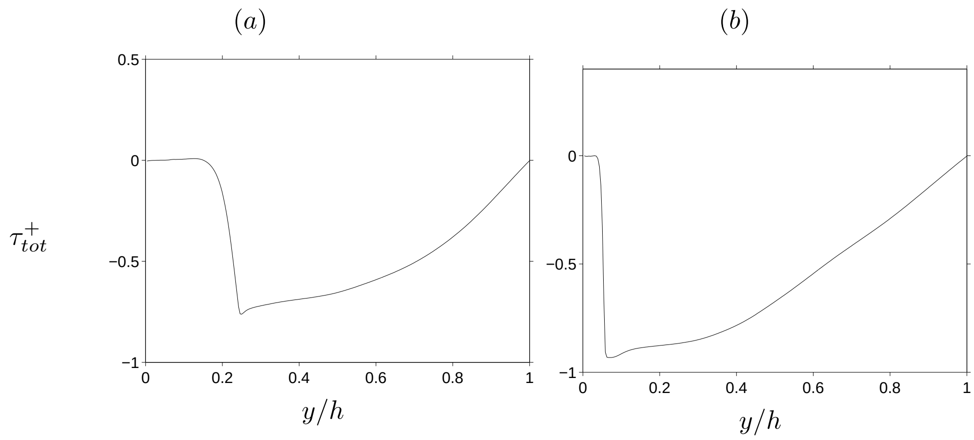

Figure 12: As figure 13, but showing the total shear stress.

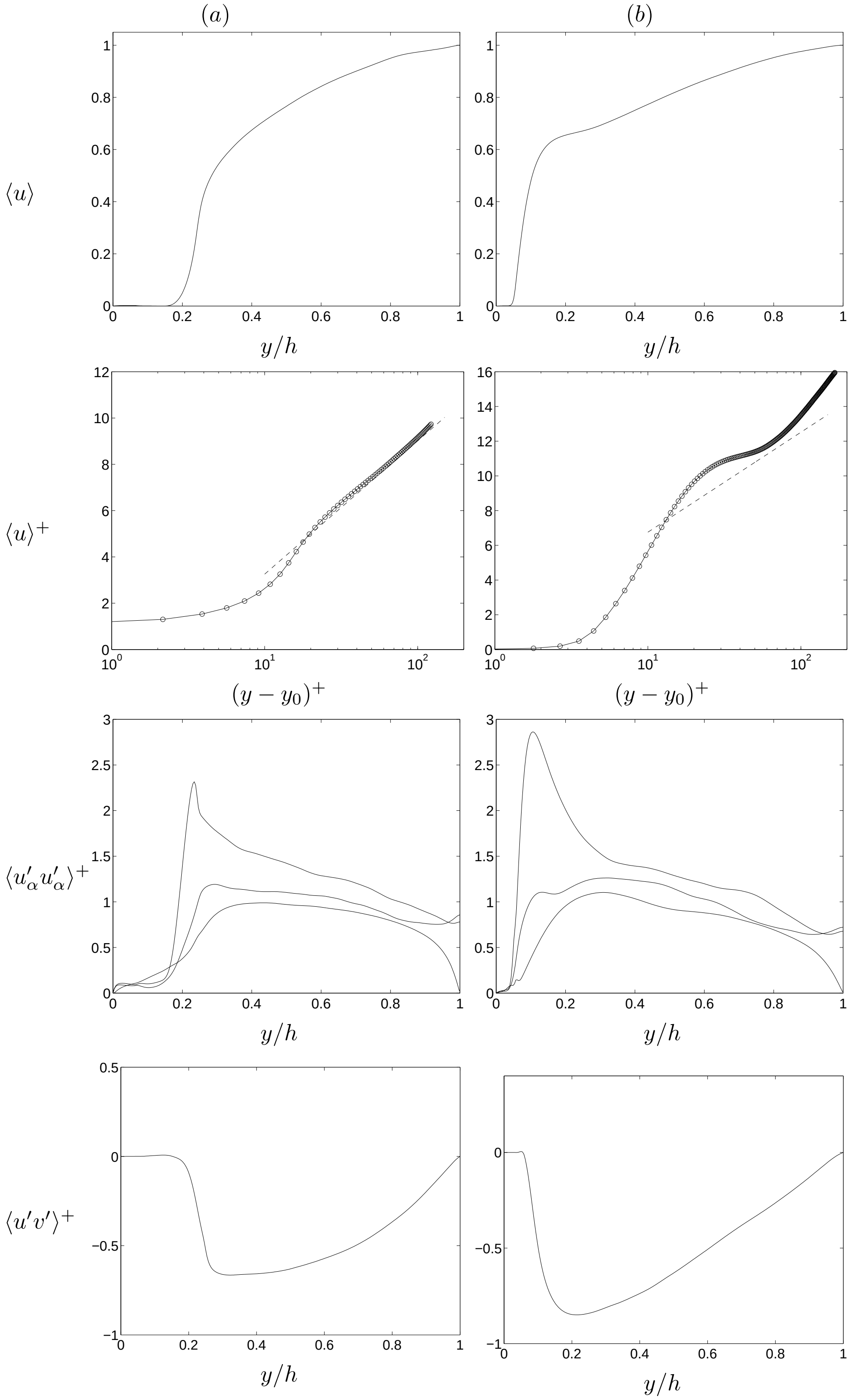

Figure 13: Statistics from the two cases of wall-mounted spheres in a half-plane channel: (a) case 13; (b) case 16. The log-law $\langle u\rangle^+ = 2.5\log((y-y_0)^+) + A$ is fitted as indicated in table 2.

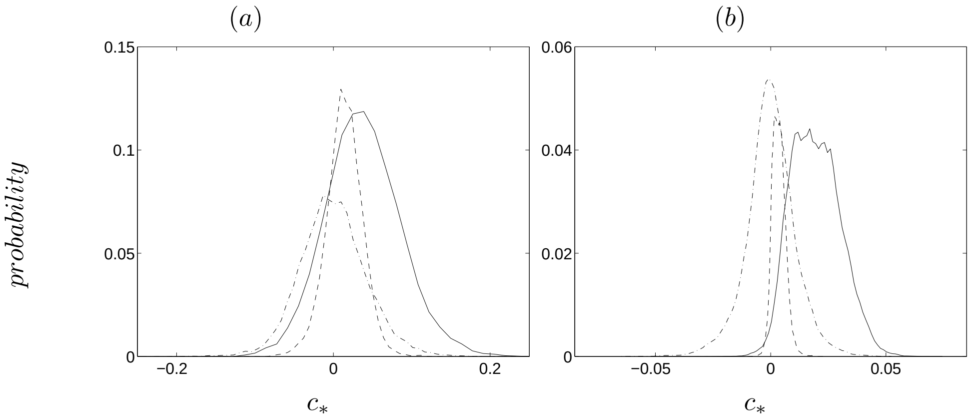

Figure 14: Normalized histograms of the three force components acting upon the top layer of spheres in the simulation of turbulent flow over spherical roughness elements: (a) case 13; (b) case 16. The lines correspond to: ——— , c_D; - - - - , c_{Ly}; —·— , c_{Lz}. Note that the coefficients are defined with the bulk velocity, e.g. $F_x = 1/2\pi D^2/4u_b^2 c_D$.

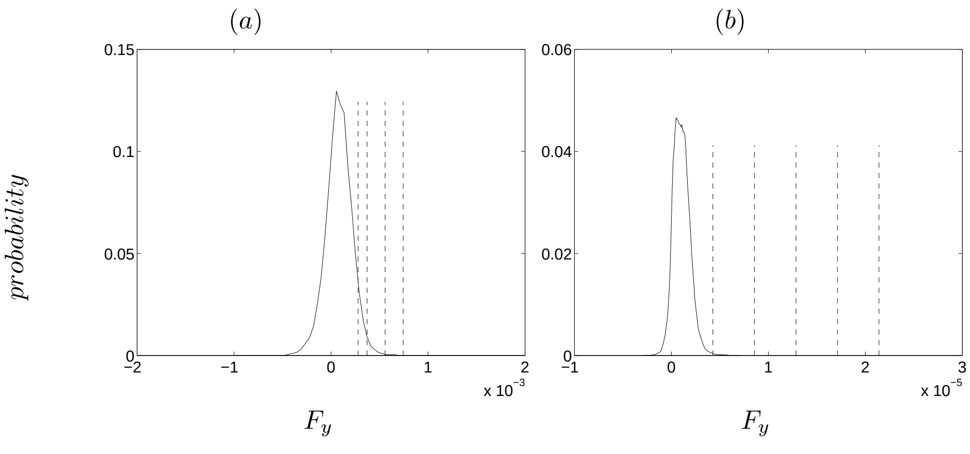

Figure 15: Normalized histograms of the lift force F_y acting upon the top layer of spheres: (a) case 13; (b) case 16. The dashed lines correspond to the gravitational forces acting upon the different particle types simulated in the erosion experiment of § 3.4.

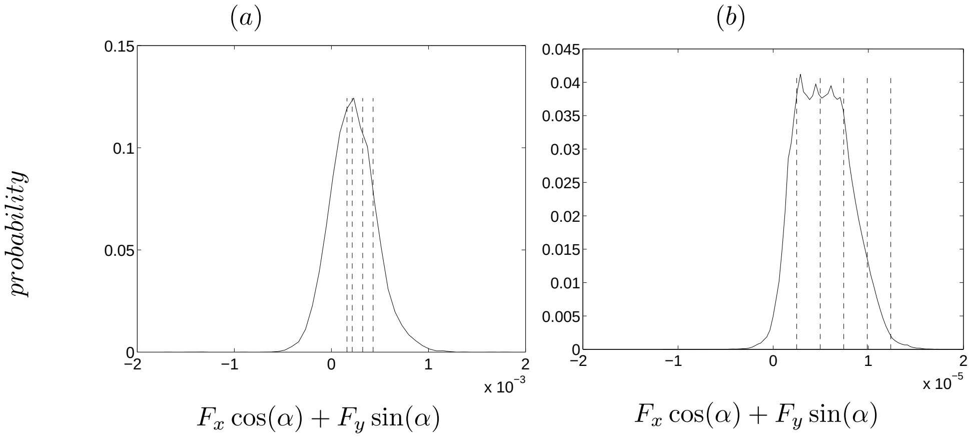

Figure 16: Normalized histograms of the hydrodynamical force components in the tangential direction at the contact points between the two layers (cf. equation 15) acting upon the top layer of spheres: (*a*) case 13; (*b*) case 16. The dashed lines correspond to the gravitational forces (projected upon the tangential direction) acting upon the different particle types simulated in the erosion experiment of § 3.4.

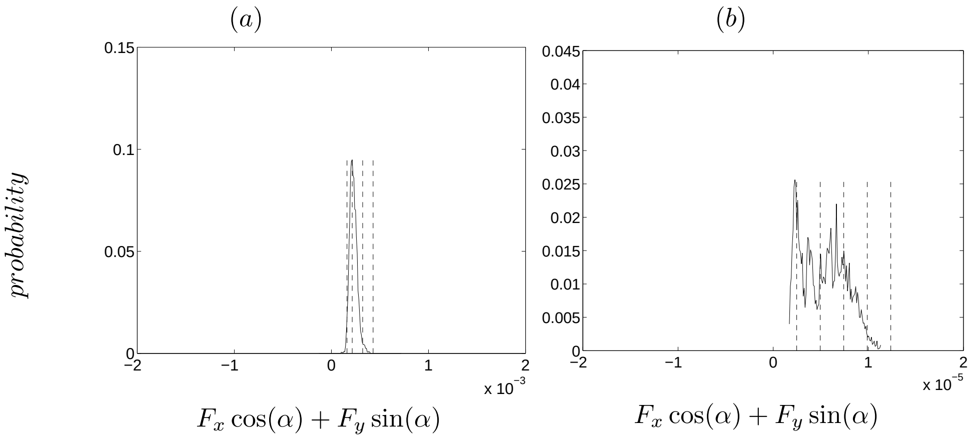

Figure 17: As figure 16, but the forces are averaged over streamwise rows of particles.

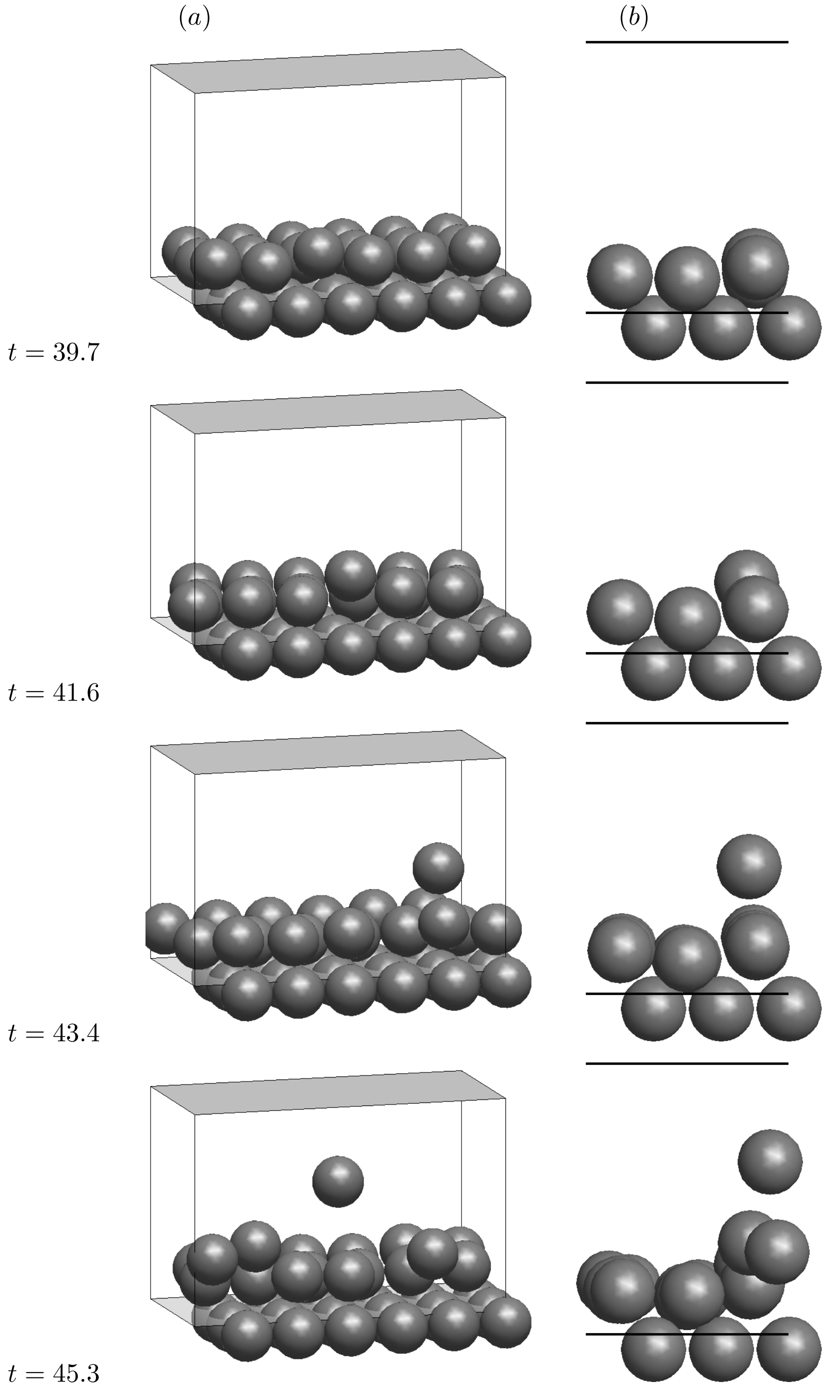

Figure 18: Particle positions during the initial stages of turbulent resuspension in case 13d. In (a), the flow is from left to right; in (b) the mean flow direction is away from the observer.

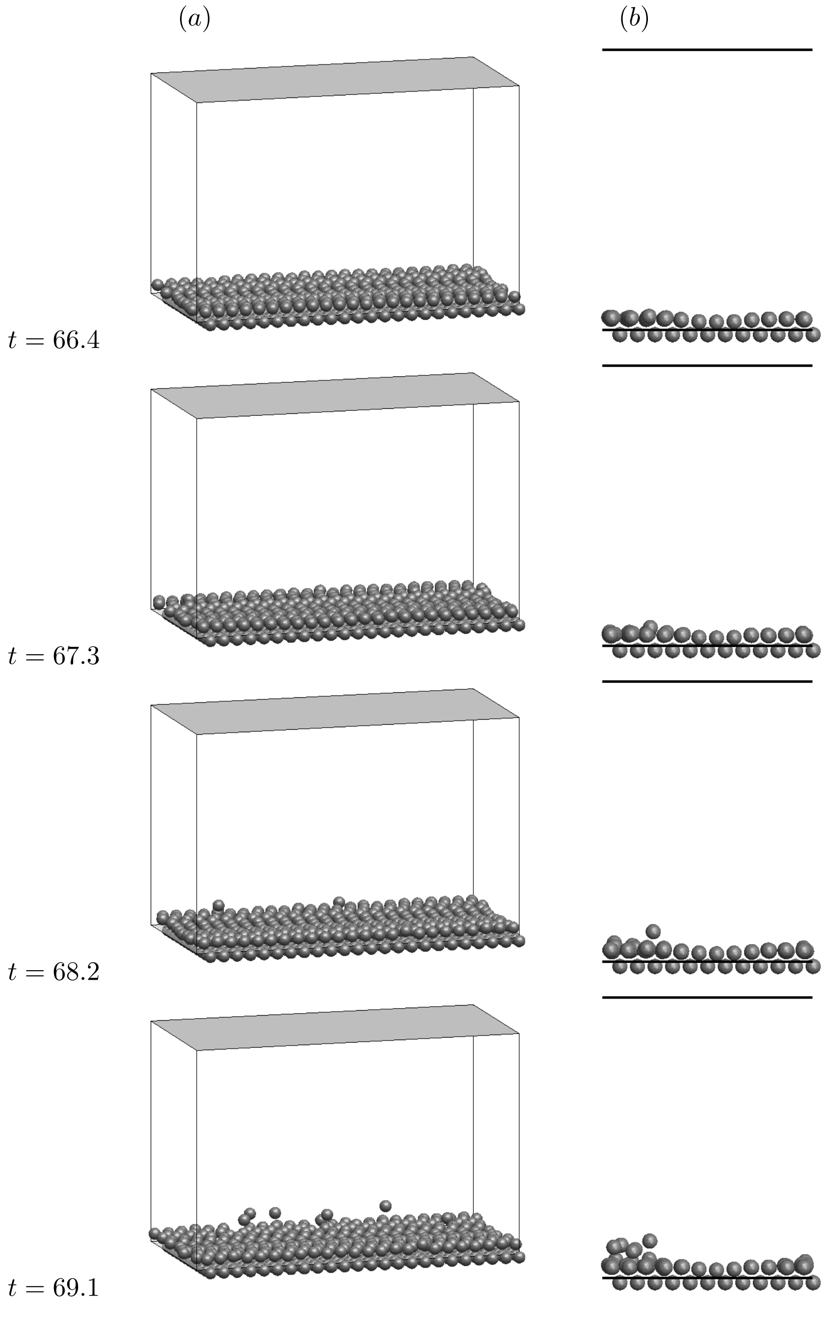

Figure 19: As figure 18, but for case 16c.

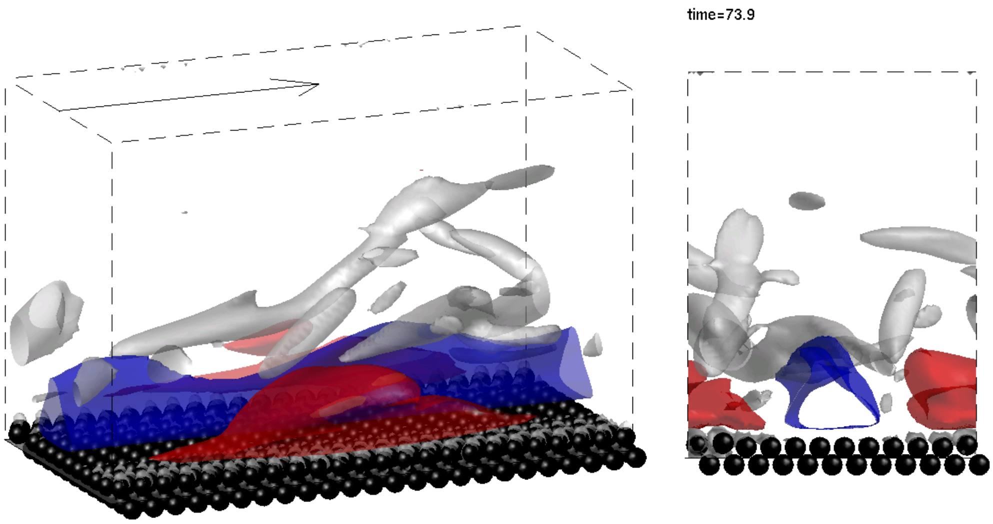

Figure 20: Flow field and particle positions at the onset of erosion in case 16f. The red (blue) surfaces indicate fluctutations of the streamwise velocity at ±0.6 times the maximum value (i.e. a pair of streaks in this case); the gray structures correspond to intense vortices detected by the λ_2 criterion of [25].

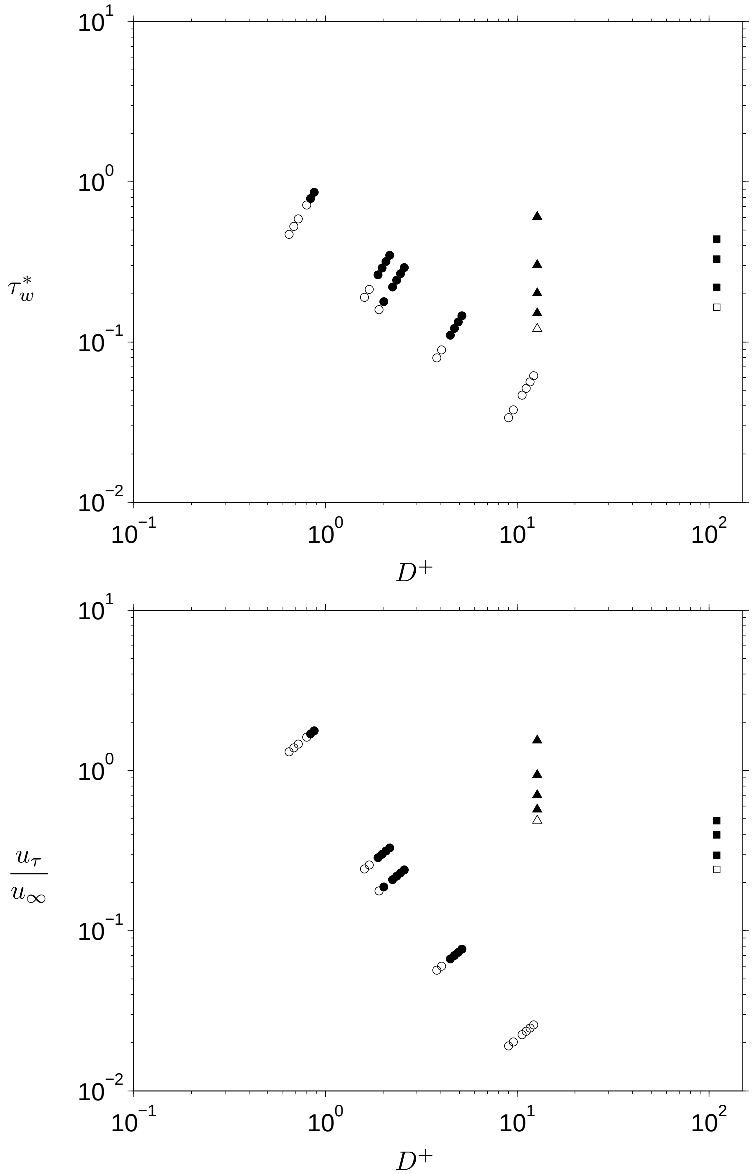

Figure 21: $\square, \blacksquare$, case 13; $\triangle, \blacktriangle$, case 16; $\circ, \bullet$, measurements from [5] for smooth walls. Filled symbols correspond to observed erosion.

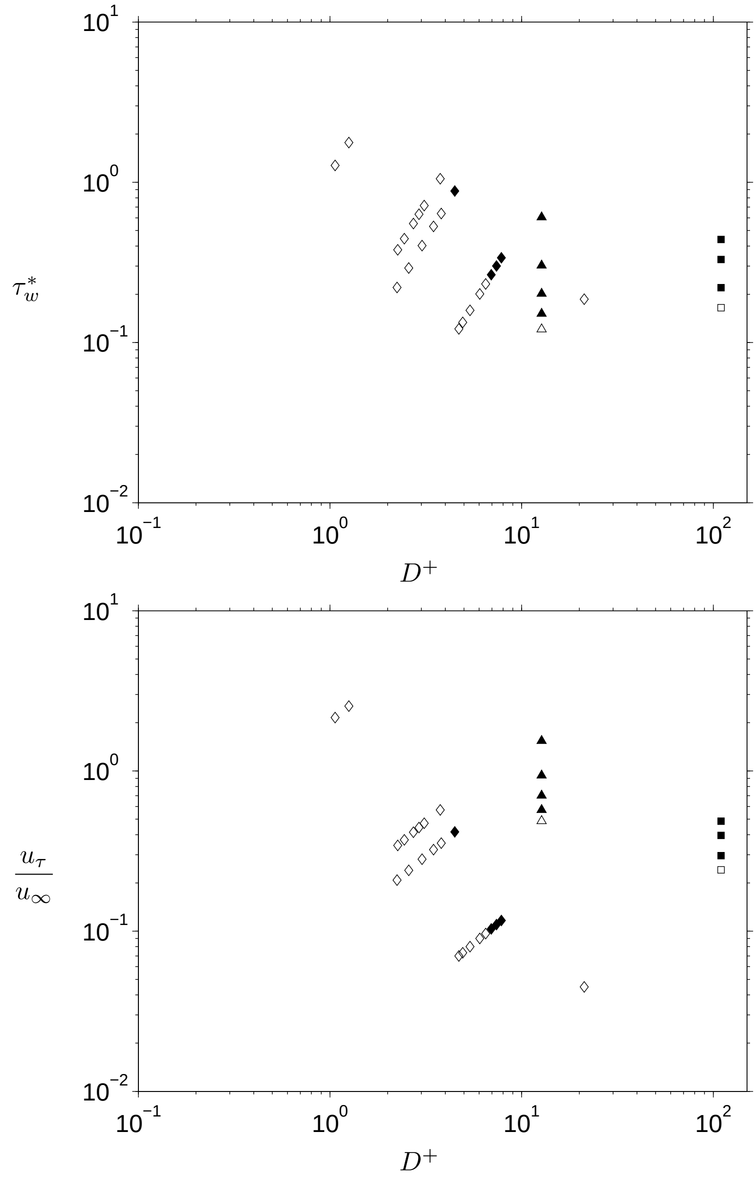

Figure 22: As figure 21, but $\Diamond$, $\blacklozenge$, correspond to measurements from [5] on rough walls.